7-1-2013

Distribution of Plasmoids in Post-Coronal Mass Ejection Current Sheets

L.-J. Guo
Dartmouth College

A. Bhattacharjee
Dartmouth College

Y.-M. Huang
Dartmouth College

The Astrophysical Journal Letters, 771:L14 (6pp), 2013 July 1 doi:10.1088/2041-8205/771/1/L14

DISTRIBUTION OF PLASMOIDS IN POST-CORONAL MASS EJECTION CURRENT SHEETS

L.-J. Guo[1,2,3,4], A. Bhattacharjee[1,2,3,4], and Y.-M. Huang[1,2,3,4]
[1] Space Science Center, University of New Hampshire, Durham, NH 03824, USA; gqa3@unh.edu, amitava@princeton.edu, yimin.huang@unh.edu
[2] Dartmouth College, Hanover, New Hampshire 03825, USA
[3] Department of Astrophysical Sciences and Princeton Plasma Physics Laboratory, Princeton University, Princeton, NJ 08540, USA
[4] Max Planck/Princeton Center for Plasma Physics, Princeton, NJ 08540, USA
Received 2013 March 26; accepted 2013 May 22; published 2013 June 19

ABSTRACT

Recently, the fragmentation of a current sheet in the high-Lundquist-number regime caused by the plasmoid instability has been proposed as a possible mechanism for fast reconnection. In this work, we investigate this scenario by comparing the distribution of plasmoids obtained from Large Angle and Spectrometric Coronagraph (LASCO) observational data of a coronal mass ejection event with a resistive magnetohydrodynamic simulation of a similar event. The LASCO/C2 data are analyzed using visual inspection, whereas the numerical data are analyzed using both visual inspection and a more precise topological method. Contrasting the observational data with numerical data analyzed with both methods, we identify a major limitation of the visual inspection method, due to the difficulty in resolving smaller plasmoids. This result raises questions about reports of log-normal distributions of plasmoids and other coherent features in the recent literature. Based on nonlinear scaling relations of the plasmoid instability, we infer a lower bound on the current sheet width, assuming the underlying mechanism of current sheet broadening is resistive diffusion.

Key words: magnetic reconnection – methods: statistical – Sun: coronal mass ejections (CMEs)

Online-only material: color figures

1. INTRODUCTION

There has been significant interest recently in the plasmoid instability, which is a super-Alfvénic secondary tearing instability of a high-Lundquist-number current sheet that leads to a new nonlinear regime of fast reconnection in which the reconnection rate becomes weakly dependent on the Lundquist number of the plasma. While the existence of this instability has been recognized for quite some time (Bulanov et al. 1979; Biskamp 1986; Lee & Fu 1986; Shibata & Tanuma 2001), the linear (Loureiro et al. 2007) and nonlinear (Lapenta 2008; Bhattacharjee et al. 2009; Cassak et al. 2009; Huang & Bhattacharjee 2010) properties of the instability, such as its precise scaling with respect to S and other plasma parameters, have been determined only recently.

The actual detection and observation of thin current sheets in a high-S coronal plasma is a formidable challenge due to the lack of adequate spatial resolution of even the most sophisticated imaging instruments. In this Letter, we demonstrate that despite this challenge, an important test of the theory by observational data can be accomplished through studies of the statistical distribution of sizes of bright moving blobs, which we interpret as plasmoids, in a post-coronal mass ejection (CME) current sheet (Sheeley & Wang 2002; Lin et al. 2005). The dynamics of bright blobs in post-CME current sheets has been studied previously. Riley et al. (2007) studied the trajectories of blobs in the current sheet during an eruption and compared Large Angle and Spectrometric Coronagraph (LASCO) observation data with a resistive magnetohydrodynamic (MHD) simulation. Song et al. (2012) performed a statistical study of blob velocities and accelerations, as well as the morphology of post-CME current sheets (or coronal rays). The reported features of blobs such as enhanced volume density and blob speeds of a fraction of Alfvén velocity are compatible with plasmoids in simulations.

Our study employs both observational data and a resistive MHD simulation of a CME event. We compare the plasmoid distributions obtained from LASCO/C2 data and simulation data, where the simulation data are analyzed with two methods. The first method is a precise topological method that utilizes the full information of the magnetic field from the simulation, and the second method is a visual inspection method that directly mimics the method of analyzing the LASCO/C2 data. We find that the second method yields a distribution that is qualitatively similar to the observational data. However, the first method yields a qualitatively different kind of distribution. Although the two methods yield similar distributions for large plasmoids, the results differ significantly for small plasmoids. This result raises questions about inferences regarding a possible log-normal distribution of coherent structures based on visual inspection alone (McKenzie & Savage 2011).

2. DISTRIBUTION OF PLASMOIDS FROM OBSERVATIONAL DATA

Here, we present observations of plasmoids from a fast CME event. The CME event occurred on 2002 January 8 17:54, after the initial eruption of the CME flux rope, a streamer-like structure was observed along the trail of CME eruption (Figure 1). Outflows and highly ionized ions were observed in the streamer-like structure, leading to a plausible inference that the streamer-like structure is a current sheet (for details, see Ko et al. 2003). During the time period 2002 January 8 21:32 to 2002 January 10 10:06, we recorded a total of 72 plasmoids in about 40 hr.

Figure 1 shows a plasmoid along with a current sheet observed in this event. To obtain the statistical data set, we record the apparent width w of each plasmoid along the direction perpendicular to the current sheet frame by frame. It is worth noting that the apparent width may be affected by projection effects, which cannot be easily quantified. Therefore, one should always be cautious in interpreting the results. Figure 2 shows the distribution of plasmoid width for this event. In Figure 2,

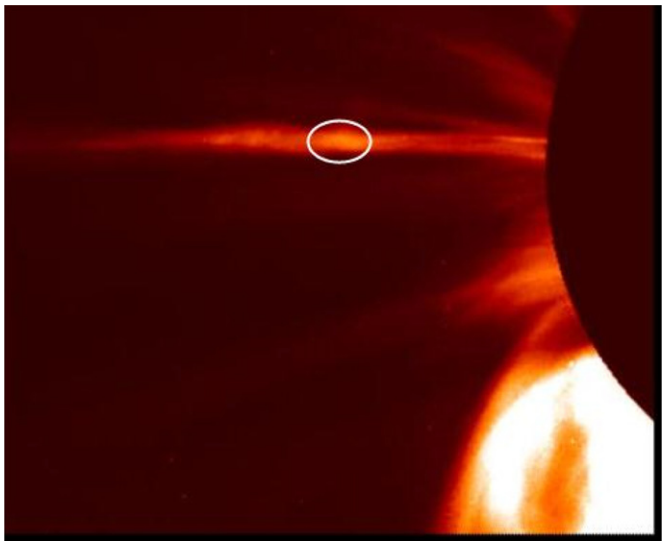

Figure 1. Current sheet fully formed 10 hr after a CME eruption, observed by LASCO on 2002 January 9 08:06 UT. The white circle marks a plasmoid in the current sheet. The plasmoid appears as a bright blob here, suggesting local density enhancement.

(A color version of this figure is available in the online journal.)

the horizontal axis represents the scale range of the observed plasmoids widths and the vertical axis shows the count of plasmoids in each scale bin. The dotted blue line shows the observational data, while the red line is the fit of an exponential function $\sim \exp(-aw)$.

The observational data manifest two distinct regimes: in the large-scale regime ($w \gtrsim 50$ Mm), the number of plasmoids in each bin decreases (as an overall trend) as w increases. This part of the distribution may be fitted with an exponential function shown on the plot. On the other hand, in the small-scale regime ($w \lesssim 50$ Mm) the number of plasmoids in each bin decreases as w decreases. The distribution over the entire range is similar to the log-normal distribution of the sizes of "tadpoles" or supra-arcade downflows (SADs) reported by McKenzie & Savage (2011). It is important to keep in mind that SADs and plasmoids are different phenomena. Observationally, SADs are regions of density depletion (McKenzie & Savage 2011), while plasmoids are structures with density enhancement. A similar trend has also been found in the distribution of flux transfer events reported by Fermo et al. (2011).

3. DISTRIBUTION OF PLASMOIDS FROM NUMERICAL SIMULATION

To compare with observations, we carry out a two-dimensional (2D) resistive MHD simulation of a CME flux rope eruption event with the Lundquist number $S = 10^5$. Here, the Lundquist number is calculated by $S = LV_A/\eta$, where the current sheet length L is typically $\sim$1 in the normalized unit, the resistivity η is a constant value 10^{-5}, and the Alfvén speed V_A in the upstream inflow region of the current sheet is typically $\sim$1. We employ a resistive MHD model with an adiabatic equation of state, and ohmic heating is included. More details about the numerical method can be found in Huang & Bhattacharjee (2010).

The simulation setup is adapted from the loss-of-equilibrium model of Forbes & Isenberg (1991). We have included gravity in our model, and the initial density is stratified such that the corona is initially in force balance. The model starts with a flux rope in equilibrium above the photosphere (Figure 3). Magnetic field lines are line-tied to the bottom of the simulation box, which represents the surface of the photosphere. As the two footpoints are pushed toward each other, magnetic energy gradually builds up. At some point, the system loses equilibrium and releases energy by changing the magnetic field configuration and ejecting a flux rope. Below the ejected flux rope,

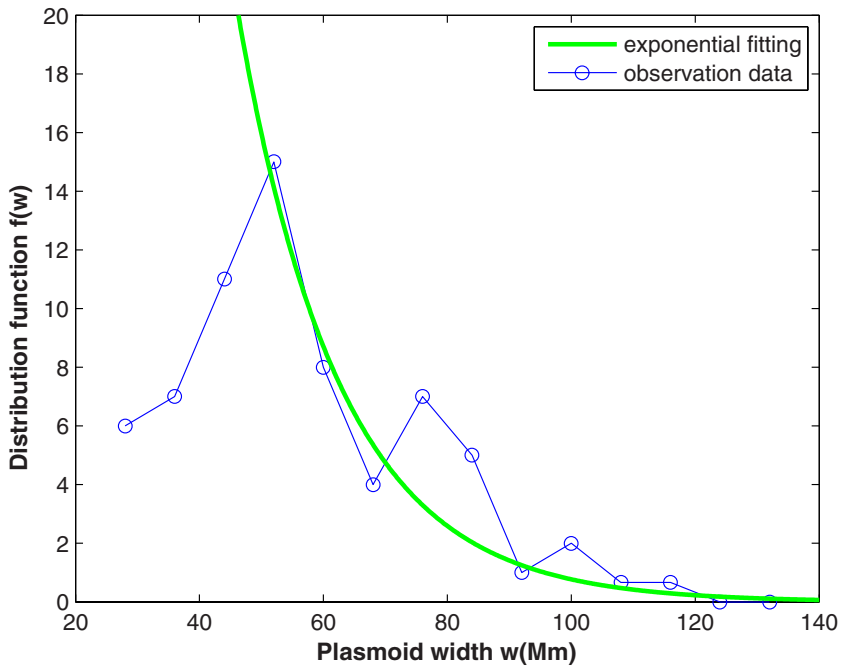

Figure 2. Plasmoid scale distribution in a CME event. The horizontal axis is the total scale range of the observed plasmoid, and the vertical axis is the count of plasmoids in each bin. The blue line with dots is our observational data set while the green line is the exponential function fitting plot.

(A color version of this figure is available in the online journal.)

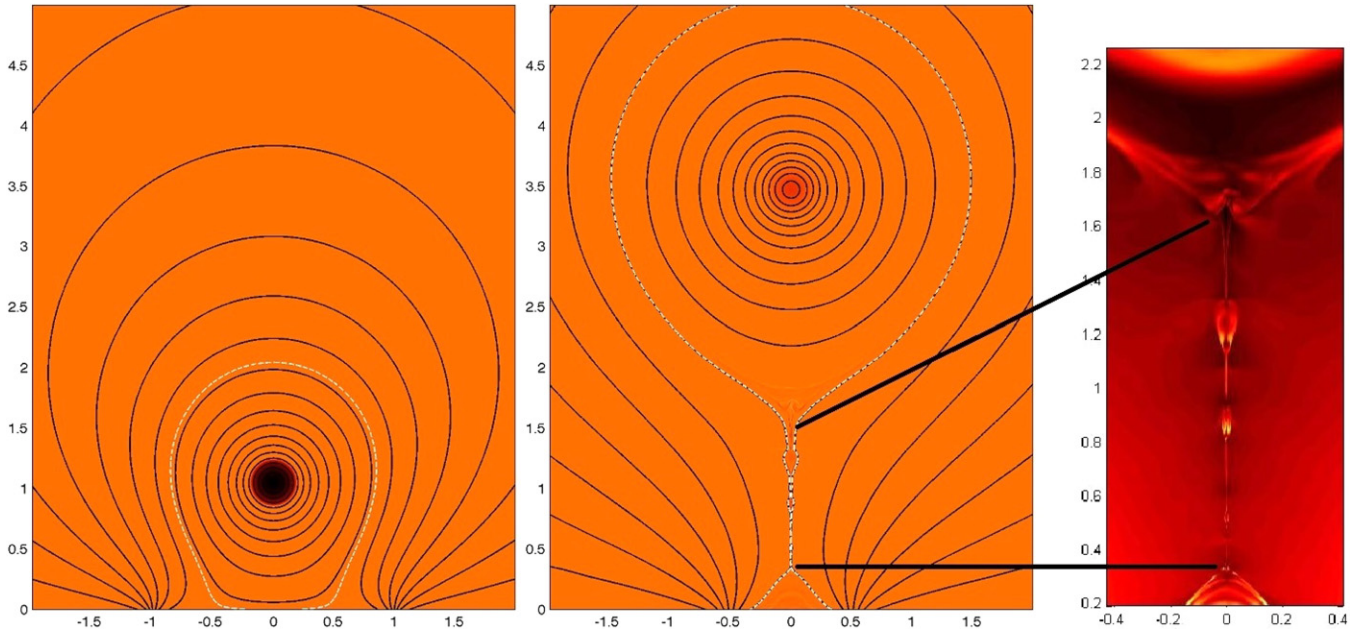

Figure 3. Left panel shows the initial state of the CME flux rope eruption model, which is a flux rope "sitting" above the photosphere in equilibrium. By pushing the two footpoints toward each other, the equilibrium is lost and the CME erupts. A thin current sheet then forms behind the CME (shown in the middle panel), connecting the CME to the cusp region above coronal loops. Here the colors represent the out-of-plane current density profile, and solid lines represent magnetic field lines. The right panel shows the detailed density image of the post-CME current sheet, where the density is color coded similarly to the LASCO observation. The large-scale current sheet is unstable and breaks into several plasmoids and shorter current sheets between plasmoids. Plasmoids appear as little blobs with enhanced density, which is represented by brightness.

(A color version of this figure is available in the online journal.)

a vertical current sheet develops (Figure 3). As the CME propagates upward, the current sheet is stretched and subsequently becomes unstable to the plasmoid instability. As a result, the extended current sheet breaks up into thinner and shorter current sheets separated by plasmoids.

The statistical data on plasmoids are obtained by two methods. In the first method, a plasmoid is identified as a magnetic O-point, and the extent of the plasmoid is determined by expanding from the O-point from one flux surface to the next (flux surfaces are tangential to the magnetic field) until the outermost flux surface is no longer a closed loop, i.e., when it has reached an X-point. This method is quantitatively accurate because the diagnostics takes into account the precise topology of the magnetic field. With this method, a total of 145 plasmoids are detected within 43 frames, and the distribution of plasmoid width is shown as the red line in Figure 4. It is fitted with an exponential distribution, shown as the green line in Figure 4. The second method is to identify plasmoids by visual inspection and to record the plasmoid scale along the direction perpendicular to the current sheet. Because the observed white-light brightness in LASCO/C2 images is linearly related to the plasma density integrated along the line of sight, this second method directly mimics the diagnostics we employ for the LASCO/C2 data. With the second method, we identify a total of 119 plasmoids within 43 frames. The blue line in Figure 4 shows the plasmoid distribution as a function of scale. The horizontal axis of Figure 4 is the plasmoid scale, assuming that the unit length in the simulation corresponds to one solar radius. Comparing Figure 4 with the distribution from observational data shown in Figure 2, we find that the data obtained by the second method (via visual inspection) and the observational data are qualitatively in good agreement. Specifically, in the large-scale regime the number of plasmoids in each bin decreases as the plasmoid width w increases, whereas in the small-scale regime the trend is the opposite. On the other hand, the distribution obtained with the first (topological) method is qualitatively different, where the number of plasmoids in each bin decreases as the plasmoid width w increases for the whole range. Although the two methods yield similar results in the large-scale regime, the first method identifies many more plasmoids than the second method in the small-scale regime. Clearly, many small plasmoids are missed by the second method. This discrepancy may be attributed to the following two reasons. First, the signature of density accumulation in a plasmoid may occur later than the formation of the plasmoid. Second, even if density accumulation is present, small plasmoids may still not be easily visible to by inspection. As a result, the smallest plasmoid size recorded by the second method is 4.7 Mm, while it is 0.3 Mm in the first method.

The statistical distribution of plasmoids is a topic of considerable theoretical interest in recent years (Fermo et al. 2010; Uzdensky et al. 2010; Huang & Bhattacharjee 2012, 2013). Huang & Bhattacharjee (2012) predicted that at high Lundquist number, the distribution of plasmoid flux ψ follows a ψ^{-1} power-law distribution, followed by an exponential tail in the large-scale regime. Although the magnetic flux ψ of a plasmoid is not directly observable from the LASCO/C2 data, under the assumption that the magnetic field B is approximately the same for different plasmoids (Uzdensky et al. 2010), we have $\psi \sim Bw$ and the distribution of plasmoids follows the same law regardless of whether ψ or w is used as the variable (see, however, the discussion in Loureiro et al. 2012). Because the observational data from LASCO/C2 and the simulation data analyzed with the second method both exhibit log-normal-like distributions, a power-law distribution at the small-scale regime would appear to be precluded. This leaves the simulation data analyzed by the first method the only one that may exhibit a power law. To reveal the distribution of small-scale plasmoids,

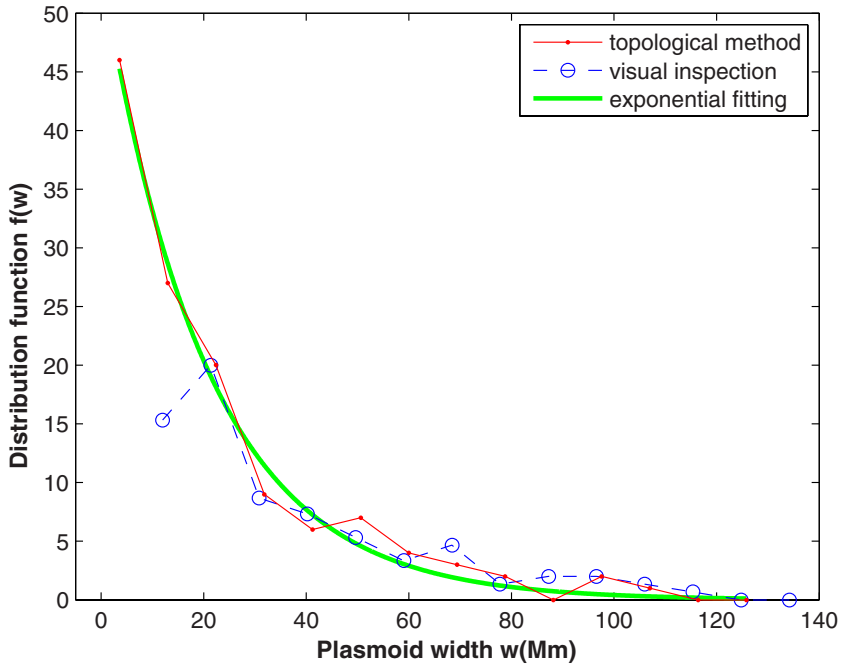

Figure 4. Plasmoid scale distribution plot from visual inspection is shown as the blue dashed line and that from the topological method as the red solid line. The exponential fitting result is shown as the green solid line. The horizontal axis is the scale range of the observed plasmoids. Here the bin size is uniform and the vertical axis is the count of plasmoids in each bin.

(A color version of this figure is available in the online journal.)

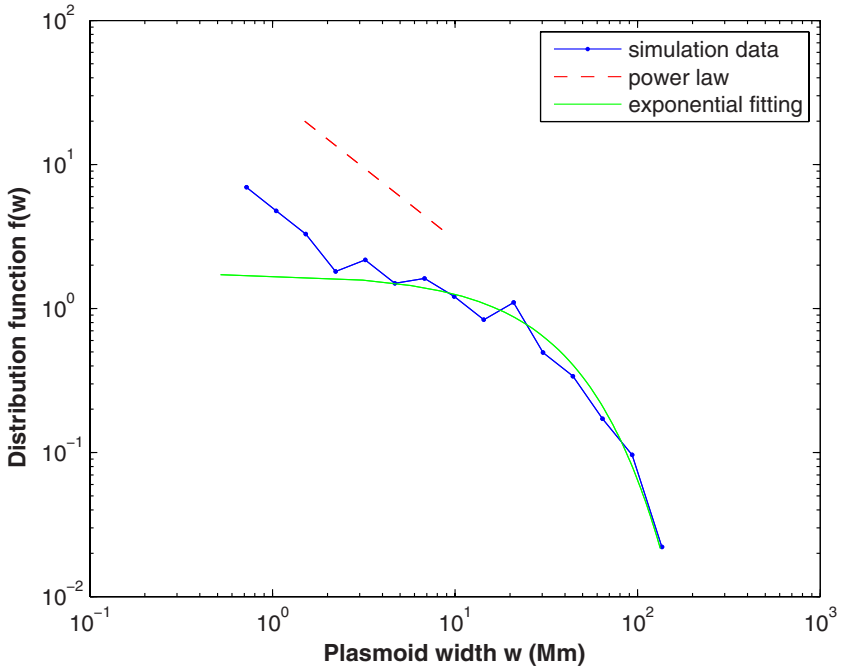

Figure 5. Plasmoid scale distribution from the topological method is shown as the blue solid line. The w^{-1} power-law distribution is shown as the red dashed line, while the exponential distribution is shown as the green solid line. The horizontal axis is the size of plasmoids, and the vertical axis is the count of plasmoids in each bin, divided by the size of the bin, which is uniform in logarithmic space.

(A color version of this figure is available in the online journal.)

we employ equally sized bins in log w instead of in w. The distribution function $f(w)$ is obtained by the number of plasmoids in each bin, divided by the size of the bin. Figure 5 shows $f(w)$ with both axes in logarithmic scale. We can see that although the distribution of large plasmoids is well fitted by the same exponential function in Figure 4 (shown as the green line), the distribution of small plasmoids clearly follows a different trend, which is close to a w^{-1} power law (shown as the red dashed line). Because the CME eruption simulation requires significantly more computational resources than idealized configurations would need, the Lundquist number $S \sim 10^5$ of this run is lower than what we were able to achieve in another study of plasmoid instability (Huang & Bhattacharjee 2012), where the highest Lundquist number is $S \sim 10^7$. The relative low

Lundquist number here limits the number of plasmoids in each snapshot and consequently the range of the power-law regime. As a result, we do not obtain a clear power-law regime as we found in Huang & Bhattacharjee (2012). With this caveat, the distribution shown in Figure 5 does allow a possible interpretation of the existence of an $f \sim w^{-1}$ power-law distribution for small plasmoids.

4. THEORETICAL ESTIMATION OF POST-CME CURRENT SHEET WIDTH

Determining the post-CME current sheet width is a topic of great interest. Past observational work (e.g., Ciaravella & Raymond 2008; Ko et al. 2003) reported the width of a post-CME current sheet to be around 10^4 km. Ciaravella & Raymond (2008) and Lin et al. (2009) found that the projection effect of observations had a limited role in enlarging the width of the observed current sheet, at most by a factor of two to three. By equating the distance between plasmoids with the wavelength of the fastest growing linear tearing mode, Lin et al. (2007, 2009) estimated the lower limit for post-CME current sheet width to be around 10^4 km. However, because the plasmoids observed in a post-CME current sheet are already in the nonlinear regime, the application of linear tearing mode theory is questionable. Here we estimate the post-CME current sheet width based on scaling laws in the nonlinear regime (Huang & Bhattacharjee 2010).

The post-CME current sheet tends to break into plasmoids and secondary current sheets if the Lundquist number exceeds a critical Lundquist number S_c. Following the heuristic argument in Huang & Bhattacharjee (2010), secondary current sheets connecting plasmoids are close to marginally stable, i.e., their lengths are close to the critical length $L_c \sim S_c\eta/V_A$. The number of plasmoids in the nonlinear regime scales as $n_p \sim L/L_c \sim S/S_c$. Consequently, the width of the Sweet–Parker current sheet can be written as $\delta_{\rm SP} \sim L/\sqrt{S} \sim \sqrt{LL_c/S_c}$. Therefore, if we know L, L_c, and S_c, we can estimate the Sweet–Parker width. Numerical simulations typically find $S_c \sim 10^4$ (Biskamp 1986; Bhattacharjee et al. 2009; Cassak et al. 2009; Huang & Bhattacharjee 2010; Loureiro et al. 2012), and the system size L for a post-CME current sheet is around 10^6 km ($\sim$1 solar radius). The critical length L_c may be estimated by the observed shortest distance (10^5 km) between two successive plasmoids at the heliocentric height of 1.53 solar radii. Because visual inspection may miss smaller plasmoids as we have discussed, this estimate of L_c should be viewed as an upper bound. By plugging L_c, L, and S_c into $\delta_{\rm SP} \sim \sqrt{LL_c/S_c}$, we estimate the upper limit of the post-CME current sheet width to be 3×10^3 km, which is smaller than the estimate from linear theory obtained by Lin et al. (2007, 2009). With the same assumption, by plugging L_c, L, and S_c into the relation $S \sim S_cL/L_c$, we may estimate the lower bound of the coronal Lundquist number to be about 10^5.

We should mention a few caveats about the analysis. First, the assumption of secondary current sheets being close to marginal stability may need further investigation; e.g., Baty (2012) recently argued that inter-plasmoid current layers should be Petschek-type with an X-point. Second, it is not possible to know the structures of blobs, such as whether they are extended or localized, along the direction of the line of sight. Two blobs that appear to be close to each other on 2D projection may be far apart in the third dimension. The analysis is based on a 2D model, whereas in reality three-dimensional (3D) effects are likely to be important.

5. CONCLUSIONS

In this Letter, we have studied the distribution of plasmoids in a post-CME current sheet by analyzing data from the *Solar and Heliospheric Observatory* observation of a CME event and a simulation of a CME eruption event. The simulation data are analyzed by both topological and visual inspection methods in order to identify plasmoids. Our principal findings are as follows.

1. The visual inspection method of the simulation data yields a distribution qualitatively similar to the distribution obtained from observational data. In both cases, the distribution function is an increasing function with respect to the plasmoid size w for small plasmoids, and the distribution function becomes a decreasing function with respect to w for large plasmoids. On the other hand, the topological method yields a distribution function that is a decreasing function with respect to w throughout the whole range. Because the topological method is mathematically precise and more accurate in determining plasmoids and their scales, the difference between two plots in the small-scale regime suggests that small-scale plasmoids are easy to miss when we count them by looking at observations. However, the second and less precise method is how we determine plasmoid scales from observational data (due to the lack of magnetic field data in corona). The discrepancy that shows up in examining the simulation data using both methods alerts us to be careful in obtaining constraints on theory from under-resolved observational data.
2. The distribution plot from the topological method can be fitted by an exponential function in the large-scale part, while the small-scale part follows a different trend that allows an interpretation of a w^{-1} power law. This appears to be consistent with the theoretical and numerical results in Huang & Bhattacharjee (2012), where it was shown that the distribution of the magnetic flux ψ of plasmoid follows a ψ^{-1} power-law distribution in small scales, followed by an exponential falloff in large scales. Because our run here was conducted with a relatively low Lundquist number $S = 10^5$, we do not obtain a clean power-law distribution in small scales as we did in the previous study (Huang & Bhattacharjee 2012), where simulations were carried out in a simple slab geometry with higher Lundquist numbers up to $S = 10^7$. However, it is evident that the distribution switches from an exponential function to a different trend at small scales (Figure 4).
3. We estimate the post-CME current sheet width via scaling laws of plasmoid instability in the nonlinear regime (Huang & Bhattacharjee 2010). The upper limit of the post-CME current sheet width is estimated to be 3×10^3 km, which is smaller than the estimate from linear theory and the reported observational value. However, the estimate is based on the 2D plasmoid instability model, and it is not clear how 3D effects might affect the result.

Our numerical simulations are based on the resistive MHD model, and the value of the Lundquist number we have used in the simulation is not inconsistent with our lower-bound estimate. However, plasmoid formation is known to be ubiquitous in that it is seen in Hall MHD (e.g., Huang et al. 2011) as well as fully kinetic simulations (e.g., Daughton et al. 2009), and the progression of the plasmoid instability in high-Lundquist-number fluid simulations inevitably carries the system to current sheet widths that are narrow enough that kinetic effects cannot

be neglected. Furthermore, our simulations are 2D, while reality begs a 3D model. For all these reasons, our model is clearly far too idealized to be taken without reservation. However, a 2D resistive MHD model may be a useful point of departure, to be refined further as observations become more precise.

This work was supported by the Department of Energy, Grant No. DE-FG02-07ER46372, under the auspice of the Center for Integrated Computation and Analysis of Reconnection and Turbulence (CICART), the National Science Foundation, Grant No. PHY-0215581 (PFC: Center for Magnetic Self-Organization in Laboratory and Astrophysical Plasmas), NASA Grant Nos. NNX09AJ86G and NNX10AC04G, and NSF Grant Nos. ATM-0802727, ATM-090315, and AGS-0962698.

REFERENCES

Baty, H. 2012, PhPl, 19, 092110
Bhattacharjee, A., Huang, Y.-M., Yang, H., & Rogers, B. 2009, PhPl, 16, 112102
Biskamp, D. 1986, PhFl, 29, 1520
Bulanov, S., Sakai, J., & Syrovtaskii, S. 1979, SvJPP, 5, 157
Cassak, P. A., Shay, M. A., & Drake, J. F. 2009, PhPl, 16, 120702
Ciaravella, A., & Raymond, J. C. 2008, ApJ, 686, 1372
Daughton, W., Roytershteyn, V., Albright, B. J., et al. 2009, PhRvL, 103, 065004
Fermo, R. L., Drake, J. F., & Swisdak, M. 2010, PhPl, 17, 010702
Fermo, R. L., Drake, J. F., Swisdak, M., & Hwang, K.-J. 2011, JGR, 116, A09226
Forbes, T. G., & Isenberg, P. A. 1991, ApJ, 373, 294
Huang, Y.-M., & Bhattacharjee, A. 2010, PhPl, 17, 062104
Huang, Y.-M., & Bhattacharjee, A. 2012, PhRvL, 109, 265002
Huang, Y.-M., & Bhattacharjee, A. 2013, PhPl, 20, 055702
Huang, Y.-M., Bhattacharjee, A., & Sullivan, B. P. 2011, PhPl, 18, 072109
Ko, Y.-K., Raymond, J. C., Lin, J., et al. 2003, ApJ, 594, 1068
Lapenta, G. 2008, PhRvL, 100, 235001
Lee, L. C., & Fu, Z. F. 1986, JGR, 91, 6807
Lin, J., Ko, Y.-K, Sui, L., et al. 2005, ApJ, 622, 1251
Lin, J., Li, J., Forbes, T. G., et al. 2007, ApJL, 658, L123
Lin, J., Li, J., Ko, Y.-K, & Raymond, J. C. 2009, ApJ, 693, 1666
Liu, R., Lee, J., Wang, T., et al. 2010, ApJL, 723, L28
Loureiro, N. F., Samtaney, R., Schekochihin, A. A., & Uzdensky, D. A. 2012, PhPl, 19, 042303
Loureiro, N. F., Schekochihin, A. A., & Cowley, S. C. 2007, PhPl, 14, 100703
McKenzie, D. E., & Savage, S. L. 2011, ApJL, 735, L6
Riley, P., Lionello, R., Mikić, Z., et al. 2007, ApJ, 655, 591
Sheeley, N. R., Jr., & Wang, Y.-M. 2002, ApJ, 579, 874
Shibata, K., & Tanuma, S. 2001, EP&S, 53, 473
Song, H. Q., Kong, X. L., Chen, Y., et al. 2012, SoPh, 276, 261
Uzdensky, D. A., Loureiro, N. F., & Schekochihin, A. A. 2010, PhRvL, 105, 235002